International Journal of Heat and Mass Transfer 178 (2021) 121621

Contents lists available at ScienceDirect

International Journal of Heat and Mass Transfer

journal homepage: www.elsevier.com/locate/hmt

Influence of immersed surface shape on the heat transfer process and flow pattern in a fluidized bed using numerical simulation.

J.I. Córcoles [a,b], A. Acosta-Iborra [c], J.A. Almendros-Ibáñez [a,b,*]

[a] Universidad de Castilla-La Mancha, E.T.S. de Ingenieros Industriales, Dpto. de Mecánica Aplicada e Ingeniería de Proyectos, Campus universitario s/n, Albacete, 02071, Spain

[b] Universidad de Castilla-La Mancha, Renewable Energy Research Institute, Section of Solar and Energy Efficiency, C/ de la Investigación s/n, Albacete, 02071, Spain

[c] Universidad Carlos III de Madrid, ISE Research Group, Thermal and Fluids Engineering Department, Avda. de la Universidad 30, Madrid, 28911 Leganés, Spain

ARTICLE INFO

Article history:
Received 22 February 2021
Revised 5 June 2021
Accepted 18 June 2021

Keywords:
Fluidized bed
Immersed surface
Computational particle fluid dynamic
Hydrodynamics
Local heat transfer coefficient

ABSTRACT

This paper presents a 2-D numerical simulation of a freely bubbling fluidized bed with immersed surfaces, using the Computational Particle Fluid Dynamics (*CPFD*) model implemented in the Barracuda commercial software. The heat transfer coefficients obtained are compared with an experimental study available in the open literature and numerical simulations based on the two-fluid model approach performed by other authors. Two different immersed surfaces, representing spherical and cylindrical geometries were studied.

The simulations results show different heat transfer mechanisms, depending on the angular position in the two immersed surface geometries studied. The time average heat transfer coefficient around the whole heat transfer surface were 25 % and 38 % lower than the experimental study, for the cylindrical and spherical surfaces, respectively. These differences are lower than the results obtained with the two-fluid model approach reported in the open literature. The numerical results indicate that CPFD-Barracuda is able to properly simulate the heat transfer and the dynamics of the bed in defluidized regions, such as on the top of an immersed surface, where the two-fluid model fails and overpredicts the heat transfer rate.

1. Introduction

The use of technologies to enhance the efficiency of heat transfer is essential in many engineering applications, such as industrial processes and energy production. One of the most widespread technologies is gas-solid fluidized beds, based on the excellent contact between gaseous and solid phases in the bubbling regime [1–5]. Fluidized beds can be utilized for thermal energy storage (*TES*), especially for thermochemical and concentrated solar energy applications [6]. To extract heat from fluidized beds, immersed surfaces can be used, such as an internal heat exchanger within the bed, mainly utilized for heat recovery, where the recirculated solids are used for heat and power generation [7]. In those cases, heat transfer occurs between solid particles and gas, as well as between both of these and the solid surface. Therefore, it is important to achieve a high bed-to-surface heat transfer coefficient in these technologies.

Several experimental studies have focused on measuring the heat transfer rate between fluidized beds and immersed tubes [8–12], concluding that there is a certain tube diameter that minimizes the heat transfer coefficient [11]. Izquierdo-Barrientos et al. [13] experimentally measured the increase in the heat transfer coefficient when a granular material with phase change material (*PCM*) is used due to its high enthalpy change when the *PCM* melts. Other works have studied the particle motion around tubes in fluidized [14–17] and moving beds [18–20]. They observed that the bubble motion around the tubes in fluidized beds influences the heat transfer coefficient. In moving beds, stagnant particle regions in the upper/lower part of the tubes reduce the heat transfer coefficient in these zones.

To improve the accuracy of predicting the heat transfer coefficient in a multiphase flow in fluidized beds with immersed surface, it is important to understand the gas-particle hydrodynamics, analysing the circulation and formation of bubbles in the region

* Corresponding author. Tel.:+34 967599200-ext:8204.
E-mail address: jose.almendros@uclm.es (J.A. Almendros-Ibáñez).

https://doi.org/10.1016/j.ijheatmasstransfer.2021.121621
0017-9310/

close to the wall tubes, as well as the particles and bubble movements around tubes. In addition, one of the key aspects regarding the use of immersed tubes is to analyse the stagnant region and the void area at the tube, along with the residence time of the granular material [21]. In this regard, experimental observation of the bubble behaviour is complicated [22], making it more difficult to obtain accurate information, especially in the regions close to the tubes. Hence, the use of techniques such as numerical simulations is required, which leads to a better understanding of the gas and the particle phase hydrodynamics, as well as predicting bubble behaviour.

A Computational Particle Fluid Dynamics (*CPFD*) model is an Eulerian-Lagrangian method that allows to numerically simulate fluidized bed behaviour in large geometries [23]. This method is based on the multiphase particle-in-cell ($MP-PIC$) method. In *CPFD*, computational particles are defined, being formed by a group of particles with the same properties, rather than for individual particles as in discrete element models (*DEM*)[24]. *CPFD* also presents higher accuracy than two-fluid models (*TFM*)[25,26], in which the results are greatly influenced by the grid size.

There are a different works in the literature that numerically studied the heat transfer process from immersed surfaces in fluidized beds, either based on *DEM* [27–31] or *TFM* [22,32–35]. Dong et al. [22] studied the effect of tube shape on the hydrodynamics and tube-to-bed heat transfer in fluidized beds using *TFM* in a 2-D geometry. They analysed two heated surfaces with the shape of a cylinder and a sphere, which were represented as a square and a circle in a 2-D model, respectively. It was found that the square influenced the hydrodynamics more than the circle, which delayed the onset of bed fluidization. They reported that for the heated cylindrical surface, the low velocity zone was larger than that for the heated spherical surface. Moreover, the tube avoided fluidized flow structure development in the region at the upstream, decreasing the bed efficiency. Around the tube sides, velocity increased because gas and particles attempted to avoid the tube structure. They also concluded that the results of the numerical model might be improved using models that consider the porosity between the packed particles around a tube. Fattahi et al. [34] performed a numerical simulation of the heat transfer coefficient around different immersed bodies in a fluidized bed, using *TFM* in an axisymmetric 2-D Cartesian model. They analysed two cases, using cylindrical and spherical immersed bodies. They reported that the heat transfer coefficient in a bubbling fluidized bed for the spherical body was higher than the cylindrical body. They also found that the particles moved more easily around the spherical surface, with better contact with the surface when compared with the cylindrical surface. Zhang and Wei [36] performed a 3-D *CPFD* simulation of bed-to-wall heat transfer between an immersed vertical tube and a gas-solid bubbling fluidized bed. They found heterogeneity in the distribution of the heat transfer coefficient around the tube surface, and reported that the simulated values of the heat transfer coefficient were smaller than the experimental ones, due to the default heat transfer coefficient correlation for the dense phase included in the *CPFD* software used [37].

Few of the aforementioned studies analysed the heat transfer process and flow pattern in a fluidized bed with an immersed surface using *CPFD* based on the $MP-PIC$ method. The aim of this paper is to show a detailed hydrodynamic and heat transfer analysis of the granular flow field in a fluidized bed with a spherical and a cylindrical immersed surface using Barracuda Virtual Reactor (v. 17.4.1), which implements the $MP-PIC$ method. The numerical results are compared with the experimental study performed by Di Natale et al. [38]. Moreover, the *CPFD* results of the time average heat transfer coefficient are compared with the results obtained by Dong et al. [22] and Fattahi et al. [34], who simulated the same geometries with *TFM*, to analyse the influence of the surface geometry on the heat transferred. This comparison will show large discrepancies between both numerical approaches in the heat transfer coefficient in defluidized zones, at the top of the heated surfaces, as it is explained in the paper, which has not been previously reported. The main results focus on explaining the gas-particle hydrodynamics and to predict the bubble behaviour, with particular attention to the particle velocity at the tube surface and the granular flow field, as well as the bed-to-wall heat transfer, analysing the local heat transfer distribution along the surface.

2. Numerical model and governing equations

The continuity and momentum equations of the $MP-PIC$ for the gas phase without interphase mass transfer are shown in Equations (1) and (2))[39,40], respectively:

$$\frac{\partial\left(\theta_f\,\rho_f\right)}{\partial t}+\nabla\cdot\left(\theta_f\,\rho_f\,\vec{u}_f\right)=0 \tag{1}$$

where θ_f is the fluid volume fraction, ρ_f is the fluid density, u_f is the gas velocity

$$\frac{\partial\left(\theta_f\,\rho_f\,\vec{u}_f\right)}{\partial t}+\nabla\cdot\left(\theta_f\,\rho_f\,\vec{u}_f\,\vec{u}_f\right)=-\nabla p-\vec{F}+\theta_f\,\rho_f\,\vec{g}+\nabla\cdot\left(\theta_f\,\tau_f\right) \tag{2}$$

where p is the fluid pressure, $\vec{F}$ is the momentum exchange rate per volume between gas and particles, g is the gravity acceleration, τ_f is the fluid stress tensor

The variable $\vec{F}$ is computed as follows (Equation (3)):

$$\vec{F}=\iiint f\left\{V_p\,\rho_p\left[D_p\left(\vec{u}_f-\vec{u}_p\right)-\frac{1}{\rho_p}\nabla p\right]+\vec{u_p}\frac{dm_p}{dt}\right\}dV_p\,d\rho_p\,d\vec{u}_p\,dT_p \tag{3}$$

where f is the particle probability distribution function, V_p is the particle volume, ρ_p is the particle density, D_p is the drag function, u_p is the particle velocity, m_p is the particle mass, and T_p is the particle temperature

According to [41], the dynamics of the particle phase is described with f, which is the function for the particle position, particle velocity, particle volume, particle density and time. The Liouville equation for the particle position without a collision model is described as follows [42]:

$$\frac{\partial f}{\partial t}+\nabla\cdot\left(f\,\vec{u}_p\right)+\nabla\vec{u}_p\cdot\left(f\,\frac{d\vec{u}_p}{dt}\right)=0 \tag{4}$$

The air density is computed using the ideal gas equation of state:

$$p=\rho_f\,R_g\,T \tag{5}$$

where R_g is the gas constant and T the absolute temperature.

The change in velocity of particle with time:

$$\frac{d\vec{u}_p}{dt}=D_p\left(\vec{u}_f-\vec{u}_p\right)-\frac{1}{\rho_p}\nabla p-\frac{1}{\theta_p\,\rho_p}\nabla\tau_p+\vec{g} \tag{6}$$

where θ_p is particle volume fraction (*PVF*), and τ_p is the particle normal stress

The particle normal stress (τ_p) is computed as follows [40]:

$$\tau_p=\frac{P_s\,\theta_p^{\beta}}{max[(\theta_{cp}-\theta_p),\varepsilon(1-\theta_p)]} \tag{7}$$

where P_s is the pressure constant, β is a constant, θ_{cp} is particle volume fraction at close packing, and ε is a constant.

The fluid-phase energy equation obtained from the fluid total energy equation [43,44] is shown in Equation (8).

$$\frac{\partial}{\partial t}\left(\theta_f \rho_f h_{fe}\right) + \nabla \cdot \left(\theta_f \rho_f h_{fe} \vec{u_f}\right) = \theta_f \left(\frac{\partial p}{\partial t} + \vec{u_f} \cdot \nabla p\right) + \Phi - \nabla \cdot (\theta_f \vec{q}) + \dot{Q} + \dot{q}_D + S_h \tag{8}$$

where h_{fe} is the fluid enthalpy, Φ is the viscous dissipation, $\vec{q}$ is the fluid heat flux, $\dot{Q}$ is an energy source per volume, $\dot{q}_D$ is the enthalpy diffusion term associated with chemical reactions, and S_h is the conservative energy exchange from the particle phase to the fluid phase. In the present study, the viscous dissipation term (Φ) is neglected and there is no energy source or chemical reactions.

Parameters $\vec{q}$ and S_h are computed as follows:

$$\vec{q} = -k_f \nabla T_f \tag{9}$$

where k_f is the fluid thermal conductivity, and T_f is the fluid temperature.

The conservative energy exchange from the particle phase to the fluid phase is calculated as follows:

$$S_h = \int\int\int f \left\{ m_p \left[D_p (\vec{u_p} - \vec{u_f})^2 - Cp_p \frac{dT_p}{dt} \right] - \frac{dm_p}{dt}\left[h_{pe} + \frac{1}{2}(\vec{u_p} - \vec{u_f})^2 \right] \right\} dm_p d\vec{u_p} dT_p \tag{10}$$

where h_{pe} is the particle enthalpy.

The particle energy equation is expressed as follows:

$$Cp_p \frac{dT_p}{dt} = \frac{1}{m_p} \frac{k_f Nu_f}{d_p} A_p (T_f - T_p) \tag{11}$$

where Nu_f is the Nusselt number for heat transfer in the fluid to the particle, d_p is the particle diameter, A_p is the projected area of the particle.

In Equation (11), the heat transfer between individual particles within a cloud of particles is not considered because the temperature differences between particles in the same cloud are not significant on account of the local temperature uniformity of particles that is achieved in fluidized beds. In addition, any heat released due to surface reactions is incorporated in the fluid-phase energy equation. With regard to the energy exchange between clouds, in the numerical model, it is taken into account indirectly with the heat transfer between gas and clouds. Therefore, if there are two adjacent clouds at different temperatures, the hot cloud transfers energy to the fluid phase and then the fluid exchanges energy with the colder adjacent cloud. This heat transfer is governed by the fluid-to-particle heat transfer coefficient (h_{fp}, Equation (24)), that is explained later.

2.1. Drag model

With regard to the drag model, the drag force exerted on the particle (F_p), used in Equation (3) depends on the fluid conditions, on the gas-particle drag coefficient and on the Reynolds number and can be computed as follows:

$$\vec{F_p} = m_p D_p |\vec{u_f} - \vec{u_p}| \tag{12}$$

Several models are proposed to compute the drag force on solid particles. In the present study, Wen-Yu drag model [45] was used, which is expressed as follows:

$$D_p = 0.75 C_d \frac{\rho_f |\vec{u_f} - \vec{u_p}|}{\rho_p d_p} \tag{13}$$

and

$$C_d = \frac{24}{Re}\theta_f^{-2.65} \qquad for \quad Re < 0.5 \tag{14}$$

$$C_d = \frac{24}{Re}(1 + 0.15\, Re^{0.687})\theta_f^{-2.65} \qquad for \quad 0.5 \le Re \le 1000 \tag{15}$$

$$C_d = 0.44\, \theta_f^{-2.65} \qquad for \quad Re > 1000 \tag{16}$$

where C_d is the gas-particle drag coefficient and Re is the Reynolds number

The Reynolds number is defined as:

$$Re = \frac{\rho_f |\vec{u_f} - \vec{u_p}| d_p}{\mu_f} \tag{17}$$

where μ_f is the dynamic viscosity of the fluid.

2.2. Heat transfer coefficients

Software Barracuda defines the local fluid-to-wall heat transfer coefficient (h_w)(Equation (18)) comprising two components [46], the heat transfer coefficient of the gas (h_f)(Equation (20)) and the heat transfer coefficient of the particles (h_p)(Equation (21)), weighted by a function of the particle volume fraction at the wall (f_p). In the numerical model, the heat transfer from the walls to the particles is carried out through the fluid phase, i.e. the wall transfers energy to the fluid phase, which can then transfer energy to the particles. Note that there are no terms containing the wall temperature in the particle energy equation Equation (11), which is explained because the heat transfer from the wall to the gas is governed by the heat transfer coefficient h_w (Equation (18)), that is accounted for as a source term in the fluid-phase energy equation, within the term $\dot{Q}$ of Equation (8)

$$h_w = h_f + f_p h_p \tag{18}$$

$$f_p = 1 - e^{-10\,(\theta_p/\theta_{cp})} \tag{19}$$

$$h_f = (c_0 Re_L^{n1} Pr^{n2} + c_1)\frac{k_f}{L} + c_2 \tag{20}$$

$$h_p = (c_3 Re_p^{n3})\frac{k_f}{d_p} \tag{21}$$

In Equations(18)-(21) L is the cell length, c_0, c_1, c_2, c_3, n_1, n_2 and n_3 are input model parameters. In this work, c_0, c_1, c_2 and c_3 had a value of 0.46, 3.66, 0 $W/(m^2K)$ and 0.525, respectively; n_1, n_2 and n_3 presented a value of 0.5, 0.33 and 0.75, respectively. These values correspond with the correlations proposed by Leva and Grummer [37] and Douglas and Churchill [47], as discussed in Yang [46]. These coefficients are the default values proposed by the *CPFD* software. The Reynolds numbers in Equations (20) and (21) are defined as follows:

$$Re_L = \frac{\rho_f u_f L}{\mu} \tag{22}$$

$$Re_p = \frac{\rho_f u_f d_p}{\mu} \tag{23}$$

where u_f is the local fluid velocity and it is directly computed from CPFD-Barracuda.

Heat transfer between the fluid phase and the particle phase is modelled by the fluid-to-particle heat transfer coefficient (h_{fp}), defined as follows:

$$h_{fp} = (c_4 Re^{n_4} Pr^{0.33} + c_5)\frac{k_f}{d_p} + c_6 \tag{24}$$

where c_4, c_5 and c_6 and n_4 are input coefficients with the default values of 0.37, 0.1, 0 $W/(m^2K)$ and 0.6, respectively, which properly fit the experimental data of [48].

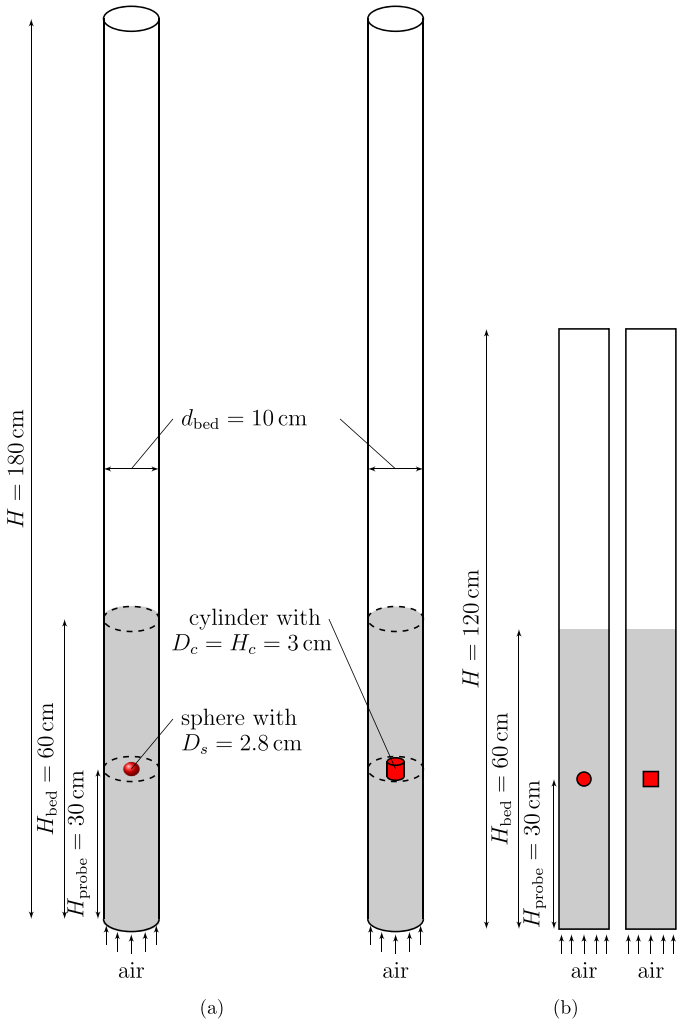

Fig. 1. 3-D geometry of the experiments carried out by Di Natale et al. [38] for the spherical and the cylindrical surfaces (a) and the equivalent 2-D schematic model used in the numerical simulations (b).

In this study, to describe the heat transfer behaviour, a time average heat transfer coefficient ($\overline{HTC}_m$) and an average heat transfer coefficient (HTC_m) have been defined as follows:

$$\overline{HTC}_m = \frac{1}{t}\int_0^t HTC_m \, \mathrm{d}t \tag{25}$$

where

$$HTC_m = \frac{1}{A_s}\int_{A_s} h_w \, \mathrm{d}A_s \tag{26}$$

where A_s is the immersed surface area.

2.3. Model setup

The geometrical and physical parameters used in the numerical simulations were similar to those in the experimental study performed by Di Natale et al. [38]. In their study, the authors analysed the effect of different surface shapes immersed into the fluidized bed on the heat transfer rate. The height (H) of the reactor was 1800 mm with an initial bed height (H_{bed}) of 600 mm. Of the possible geometries, they used a spherical probe (28 mm diameter), and a vertical cylinder (30 mm diameter and 30 mm side length), located at a height of 300 mm above the gas distributor. Fig. 1(a) shows a scheme of the geometry used in the experiments by Di Natale et al. [38].

In the present study, the computational domain was a rectangular numerical model with each probe immersed into the fluidized bed as shown in Fig. 1(b). In this case, to reduce the computational cost, the height of the reactor used was 1200 mm, with a width of 100 mm at the inlet. A scaled thickness (15 mm) was implemented in the model, so the cases were actually approximated to a 2-D model. Moreover, the spherical probe and the vertical cylinder were modelled as a circle (28 mm diameter) and a square (30 mm side), respectively, as performed by Dong et al. [22]. Although the experimental facility was 3-D, the numerical model was selected 2-D as a first approximation it permits to visualize more clearly the differences in the flow and in the heat transfer coefficient related to the different geometries (spherical and cylindrical) and also to quantitative compare with the results obtained by other researchers [22,34] with the same 2-D geometry using the *TFM* approach.

In the present study, two different mesh sizes (Grid 1 and Grid 2) were analysed, as shown in Fig. 2. Grid 1 consisted of an uniform mesh in all directions, with a quadrangular cell size of 2.8×10^{-3} m, resulting in 74,000 cells in both geometries. Grid 2 consisted of 138,000 (spherical shape) and 135,000 (cylindrical shape) cells, with a refined mesh in the region close to the immersed surface. This resulted in a general quadrangular domain, where the largest quadrangular cells had a size of 2.8×10^{-3} m and the smallest ones of 1.4×10^{-3} m. A few cells (i.e. 5) were defined along the bed thickness direction in both grids. Information about the grids used is shown in Table 1.

The main parameters for the numerical simulation are defined in Table 2. The fluidizing material used for the bed was glass beads, with a uniform diameter (0.5 mm) and initial particle volume fraction at close packing (θ_{cp}) of 0.6, real density of 2540 kg/m^3 and sphericity (Ψ_p) of 1. To fluidize the bed, compressible air enters the domain through the bottom inlet of the bed, considering an isothermal flow temperature of 293 K and pressure inlet of 103000 Pa. A uniform superficial gas velocity of 0.3 m/s was defined, about 1.4 times the minimum fluidization velocity (u_{mf})(fully bubbling fluidized bed), which was obtained by pressure drop measures and visual observations, according to Di Natale et al. [38]. Air leaves the bed through the top outlet, which is connected to the exterior air at atmospheric conditions (20 °C and 100000 Pa). For the gas, a non-slip condition was defined at the immersed surface and lateral walls. The bed walls were defined as adiabatic, and the walls of the immersed surfaces had a constant temperature (373 K).

The particle to wall interaction was defined with the default values parameters for normal to wall momentum retention (0.85) and tangent to wall momentum retention (0.85), whose values correspond to hard particle material [49] as well as the diffuse bounce (5), which defines that particles will have a scattered angle distribution after hitting the wall [3]. The retention or restitution coefficients represent the fraction of the particle momentum (normal- or tangent-to-wall) that is retained after a collision with the wall. To compute particle to particle interaction, the values for the constants P_s (1), ε (10^{-8}) and β (3) (Equation (7)) were set to the default [2,50].

The numerical setup and conditions are similar to those proposed by Dong et al. [22] and Fattahi et al. [34],who used a *TFM* in the same geometry. The initial and boundary conditions of both studies are shown in Table 3. The wall surface constant temperature of 373 K is the same thermal condition defined by Dong et al. [22] and Fattahi et al. [34].

The simulation time was 60 seconds, which was determined to be long enough to reach a stable value of the heat transfer coefficient around the two surfaces analysed. Longer times do not change the time average value and only increase the computational time. The time-averaged values during $t = 5$ s up to $t = 60$ s were

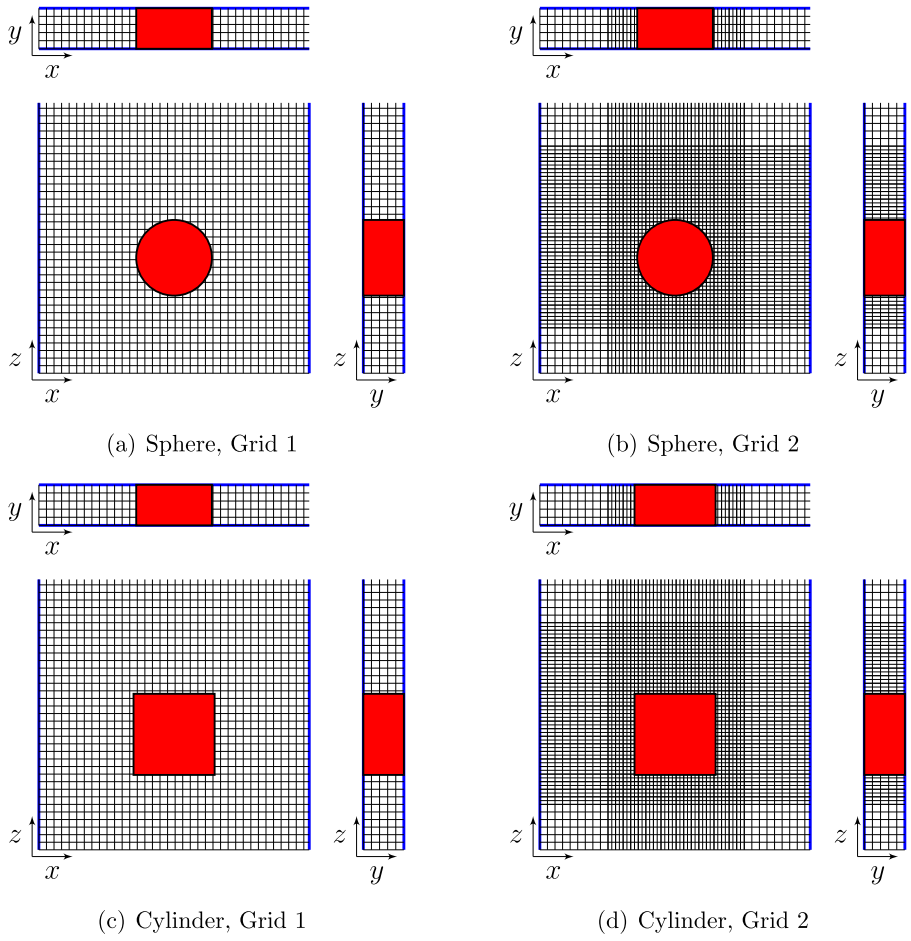

Fig. 2. Grids of the fluidized bed studied for the spherical and cylindrical surfaces.

Table 1
Cell and computational parameters for the studied cases

Tube	*Grid*	Δt [s]	$N_{\text{comput. parcels}}$	$N_{\text{comput. particles}}$	N_{cells}	$N_{\text{comput. particles in each parcel}}$	*Computational time* [s]
Spherical	Grid 1	10^{-4}	1.358×10^6	8.147×10^6	74,060	5.99	4.139×10^5
Spherical	Grid 2	10^{-4}	2.758×10^6	8.155×10^6	138,230	2.95	9.447×10^5
Cylindrical	Grid 1	10^{-4}	1.365×10^6	8.127×10^6	74,450	5.99	4.438×10^5
Cylindrical	Grid 2	10^{-4}	2.752×10^6	8.115×10^6	134,880	2.95	9.465×10^5

Table 2
Initial and boundary conditions for the numerical simulation.

Particle type	Glass beads	
Particle diameter (d_p, mm)	0.5	
Particle temperature (T_p, K)	293	
Particle density ($\rho_p, kg\,m^{-3}$)	2540	
Particle specific heat ($Cp_p, J\,kg^{-1}\,K^{-1}$)	765	
Particle thermal conductivity ($k_p, W\,m^{-1}\,K^{-1}$)	0.9	
Initial particle volume fraction at close packing (θ_{cp})	0.6	
Particle sphericity (Ψ_p)	1	
Inlet	Gas velocity ($u_f, m\,s^{-1}$)	0.3
	Fluid temperature (T_f, K)	293
Outlet	Pressure outlet (P_{out}, Pa)	100000
Walls	Wall bed temperature (T_{wb}, K)	Adiabatic
	Wall immersed surface constant temperature (T_s, K)	373
	Non-slip for gas	
	Particle to wall interaction:	
	Normal-to-wall retention coefficient	0.85
	Tangent-to-wall retention coefficient	0.85
	Diffuse bounce	5

Table 3
Initial and boundary conditions of *TFM* model

	Dong et al. [22]	Fattahi et al. [34]
Height(H, mm)	1200	1200
Width(W, mm)	100	100
Initial bed height(H_{bed}, mm)	600	600
Particle diameter (d_p, mm)	0.5	0.5
Particle density ($\rho_p, kg\,m^{-3}$)	2540	2540
Fluid density ($\rho_f, kg\,m^{-3}$)	1.225	1.225
Particle temperature (T_p, K)	293	293
Fluid temperature (T_f, K)	293	293
Particle specific heat ($Cp_p, J\,kg^{-1}\,K^{-1}$)	765	765
Fluid specific heat ($Cp_f, J\,kg^{-1}\,K^{-1}$)	994	994
Particle thermal conductivity ($k_p, W\,m^{-1}\,K^{-1}$)	0.9	0.9
Fluid thermal conductivity ($k_f, W\,m^{-1}\,K^{-1}$)	0.0252	0.0252
Inlet velocity ($u_f, m\,s^{-1}$)	0.3	0.45
Wall immersed surface constant temperature (T_s, K)	373	373
Particle-particle restitution coefficient ($e_s, -$)	0.9	0.9
Wall to particle restitution coefficient ($e_w, -$)	0.9	0.9
Initial particle volume fraction at close packing (θ_{cp})	0.6	0.6
Particle sphericity (Ψ_p)	1	1
Inlet	Velocity inlet	Velocity inlet
Outlet	Pressure outlet	Pressure outlet
Walls	Adiabatic. No slip for gas and solids phases	Adiabatic. No slip for gas and solids phases

Table 4
Time average heat transfer coefficient at each case and grid.

Tube	*Grid*	*Experimental* $\overline{HTC}_m$ $[W/m^2\,K]$[38]	*Simulated* $\overline{HTC}_m$ *complete surface* $[W/m^2K]$	*Simulated* $\overline{HTC}_m$ *without complete surface* $[W/m^2K]$	*Simulated* $\overline{HTC}_m$ $[W/m^2K]$[22]	*Simulated* $\overline{HTC}_m$ $[W/m^2K]$[34]
Spherical	Grid 1	260	137.15	158.77	380	546/620
Spherical	Grid 2	260	138.77	158.67	380	546/620
Cylindrical	Grid 1	200	135.93	152.75	401	470/590
Cylindrical	Grid 2	200	136.21	149.20	401	470/590

considered to obtain mean values parameters, as the first 5 seconds were discarded to eliminate the large transient start-up effects from the time-averaged results of the bed. Results did not appreciably changed for longer averaging-times and were considered insensitive to the transient start-up of the fluidized bed. A time step of 10^{-4} s was used for the time period of 60 s. The simulation model was performed on a 2.1 GHz computer with CPU ES-2620 v4 and 32 GB RAM.

3. Results and discussion

3.1. Grid analysis

To maintain a compromise between stability, accuracy, and speed of the calculation, the CPFD-Barracuda software recommends a Courant-Friedrichs-Lewy (*CFL*) number of between 0.8 and 1.5. If the *CFL* during the simulations reaches a value higher than 1.5, CPFD-Barracuda automatically reduces the time step for getting $CFL = 0.8$. In all cases, *CFL* ranged from 0.2 to 1.5, where in some periods *CFL* was maintained below 1.5 and in other periods it was not modified by the software because it was below 1.5. Considering Grid 1, *CFL* ranged from 0.2 to 0.6, for the spherical probe, and 0.2 to 1, for the cylindrical probe. For Grid 2, in both cases, *CFL* ranged from 0.2 to 1.5, where in some periods *CFL* was maintained below 1.5 and in other periods it was not modified by the software because it was below 1.5.

In addition, to select the grid size used to analyse the flow behaviour, the simulated results of the $\overline{HTC}_m$ were compared to the experimental results obtained by Di Natale et al. [38]. Table 4 shows the results obtained with the two proposed grids for the spherical and the cylindrical surfaces. In the present study, the simulated $\overline{HTC}_m$ along the complete spherical and cylindrical surface was highly similar in the four analysed grids, reporting values close to 140 W/m^2K. In the experimental study carried out by Di Natale et al. [38] these values were $\overline{HTC}_m = 260$ W/m^2K(spherical) and $\overline{HTC}_m = 200$ W/m^2K(cylindrical). To compare these values, it should be noted that in Di Natale et al. [38], not all the surface of the probe is considered, because a cylindrical heater cartridge is placed at the top of the surface. So, to compute the simulated $\overline{HTC}_m$, values located in that region were not considered. Hence, the numerical simulations reported somewhat similar values for all the proposed grids, but slightly higher for the spherical surface than for the cylindrical one. Comparing these results with the ones obtained in other studies based on *TFM* of the same experimental setup, some differences should be highlighted. Dong et al. [22], performing a 2-D numerical simulation, for a 10 s simulation time, reported a simulated $\overline{HTC}_m$ for the cylindrical (401 W/m^2K) surface higher than the spherical one (380 W/m^2K), which overpredicted the $\overline{HTC}_m$. The authors reported that it was related to the effective thermal conductivity correlations when using the actual gas volume fraction, where they used a porosity model to take into account the gas pockets between the particles because a correlation did not exist for a submerged surface due to the unpredictable bubble hydrodynamics. Fattahi et al. [34] also analysed the same experimental geometry with *TFM* but with an inlet constant velocity (0.45 m/s) slightly higher than the one used in the present study. The authors reported the influence of the numerical model geometry where they used two models for the spherical and the cylindrical surfaces, a 2-D Cartesian model and an axisymmetric model. Considering a isothermal boundary condition of 373 K, the authors reported overpredicted values for $\overline{HTC}_m$ in comparison to the experimental values of Di Natale et al. [38], obtaining $\overline{HTC}_m$ of 546 W/m^2K (spherical surface) and 470 W/m^2K (cylindrical surface), using a 2-D Cartesian model and 620 W/m^2K and 590 W/m^2K, respectively, with an axisymmetric model. They explained such differences might be improved by modifying the size of the

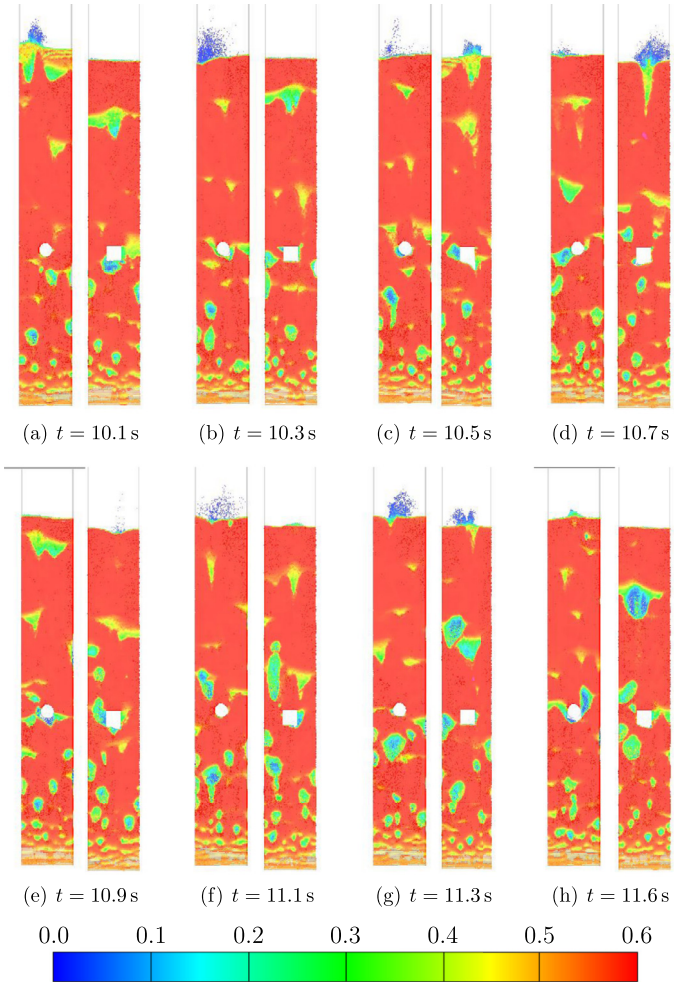

Fig. 3. Particle volume fraction during the fluidization process for the spherical and cylindrical surfaces.

grid near the wall. In their study, the authors also reported that no differences were obtained for the hydrodynamics of the bubbling fluidized bed and the main differences were obtained to predict $\overline{HTC}_m$, while the use of the axisymmetric model reported better numerical $\overline{HTC}_m$ than the 2-D model, because it takes into account the correct spherical and cylindrical surfaces.

The results obtained for the two grids analysed are highly similar in both surfaces. Grid 2 was selected to better explain the hydrodynamics and heat transfer for the analysed cases. Although the computational time to simulate 60 s of the real operation was 5 and 9 days with Grid 1 and Grid 2, respectively, we considered it not to be a significant reduction of the computing time, and the refined grid might help obtain more accurate results. This is related to better capturing the flow behaviour in the regions close to the wall surface. This was also reported by Liang et al. [2], when validating a *CPFD* model in bubbling fluidized beds, indicating that uniform mesh might not be small enough to capture the wall effect on local hydrodynamics. They also improved their numerical results using near-wall mesh refinement, especially for the mean particle velocity and the particle volume fraction.

3.2. Hydrodynamics and heat transfer

To analyse the flow pattern along the bed, the particle volume fraction (*PVF*) over approximately 2 seconds is shown in Fig. 3, where the bubbling formation during the fluidization process is shown. The bed bubbles move upwards, and large bubbles are formed moving around the spherical and the cylindrical probe surfaces, resulting in an asymmetric and oscillatory particle behaviour, as well as the expansion of particles at the bed surface due to the bubble eruption, notably observed at t = 10.1 s, t = 10.3 s, t = 11.1 s and t = 11.3 s, for the spherical surface and at t = 10.5 s, t = 10.7 s and t = 11.3 s for the cylindrical surface. It is worth noting that the bubbles detach faster from the spherical surface than from the cylindrical one, which makes it more difficult for the air to move. Moreover, observing the height of the bed, it can be seen that the bubbles move faster at the spherical surface, showing the influence of the surface shape on the bubble formation. These findings were also reported by Dong et al. [22]. In any event, the *PVF* contours did not show great differences for either the spherical or the cylindrical surfaces, as indicated by Fattahi et al. [34].

Figs. 4 and 5 show, in blue lines, the instantaneous heat transfer coefficient, particle volume fraction and particle velocity at different angular positions: on the right ($\omega = 0^\circ$), on the top ($\omega = 90^\circ$) and on the bottom ($\omega = 270^\circ$) of the tube, for the spherical and the cylindrical surfaces, respectively. The red line in these figures shows the centred moving mean every one second of simulation. The differences in the *HTC* are clearly observed, depending on the angular position of the tube. On the top of the tube ($\omega = 90^\circ$), there are almost no variations in the *PVF* and in the particle velocity, which are approximately constant and equal to $PVF \approx 0.6$ and $|\vec{u}_p| \approx 0$. The *HTC* is low because in this region of the tube there is no renovation of the particles, which remain at rest in the tube. At the beginning of the simulation (for $t \leq 20$ s) the *HTC* is higher because the static particles are cold and the heat is transferred by conduction. At the beginning, the temperature gradient is high, but this gradient decreases as the particles are heated, and consequently the *HTC* decreases. The *HTC* at $\omega = 0^\circ$ and 270° is similar in value, although at 270° there appear to be more fluctuations in this coefficient. The *PVF* at $\omega = 270^\circ$ is lower than at $\omega = 0^\circ$ in both cases. This suggests that the particle-bubble hydrodynamics around the tube, which controls the heat transfer rate, is different depending on the angular position. At one side of the tube ($\omega = 0^\circ$) a chain of bubbles is continuously passing, moving groups of compacted particles between bubbles with high velocities. These groups of high velocity particles are continuously being removed from the tube surface, assuring a good heat transfer dissipation in this zone. On the bottom of the surface ($\omega = 270^\circ$), the low particle velocities suggest that bubbles deviate from this region to the tube side and only some less compact particles from the wake of the bubble enter into contact with the bottom of the tube. Regarding the *PVF* distribution, this tendency was similar to the results reported by Dong et al. [22], although they only showed the results at 5, 6 and 7 seconds of the simulation time.

Figs. 6 and 7 show a detail of Figs. 4 and 5 over 1.5 seconds (between 10.1 and 11.6 s) for the spherical and the cylindrical surfaces, respectively. Fig. 6(a) shows that in the case of the sphere with $\omega = 0^\circ$, 3 periods (from 1 to 3) can be distinguished in which $PVF \approx 0.6$ and $u_p \approx 0\,\mathrm{m/s}$. In these periods, the *HTC* remains approximately constant with a value of $180\,\mathrm{W/(m^2\,K)}$. These values indicate that the dense phase is in contact with the heat transfer surface and the particles moves slowly. Between these periods, the bubble action makes the *PVF* decrease and the particle velocity augment, with the *HTC* increasing at certain times. At the top of the surface ($\omega = 90^\circ$), the *PVF* remains constant and equal to 0.6 while the particle velocity is null, except in periods 4 and 5, in which a small variation of u_p produces a small increase in the *HTC*. Nevertheless, the value of the *HTC* is very low across the whole period. When $\omega = 270^\circ$ (at the bottom of the surface), the behaviour is entirely different to $\omega = 0^\circ$. Fig. 6(c) indicates six periods (numbers 6 to 11) where $PVF \approx u_p \approx 0$. These values suggest that the bottom of the surface is mainly in contact with particle-free gas bubbles. At the end of each period, a peak appears

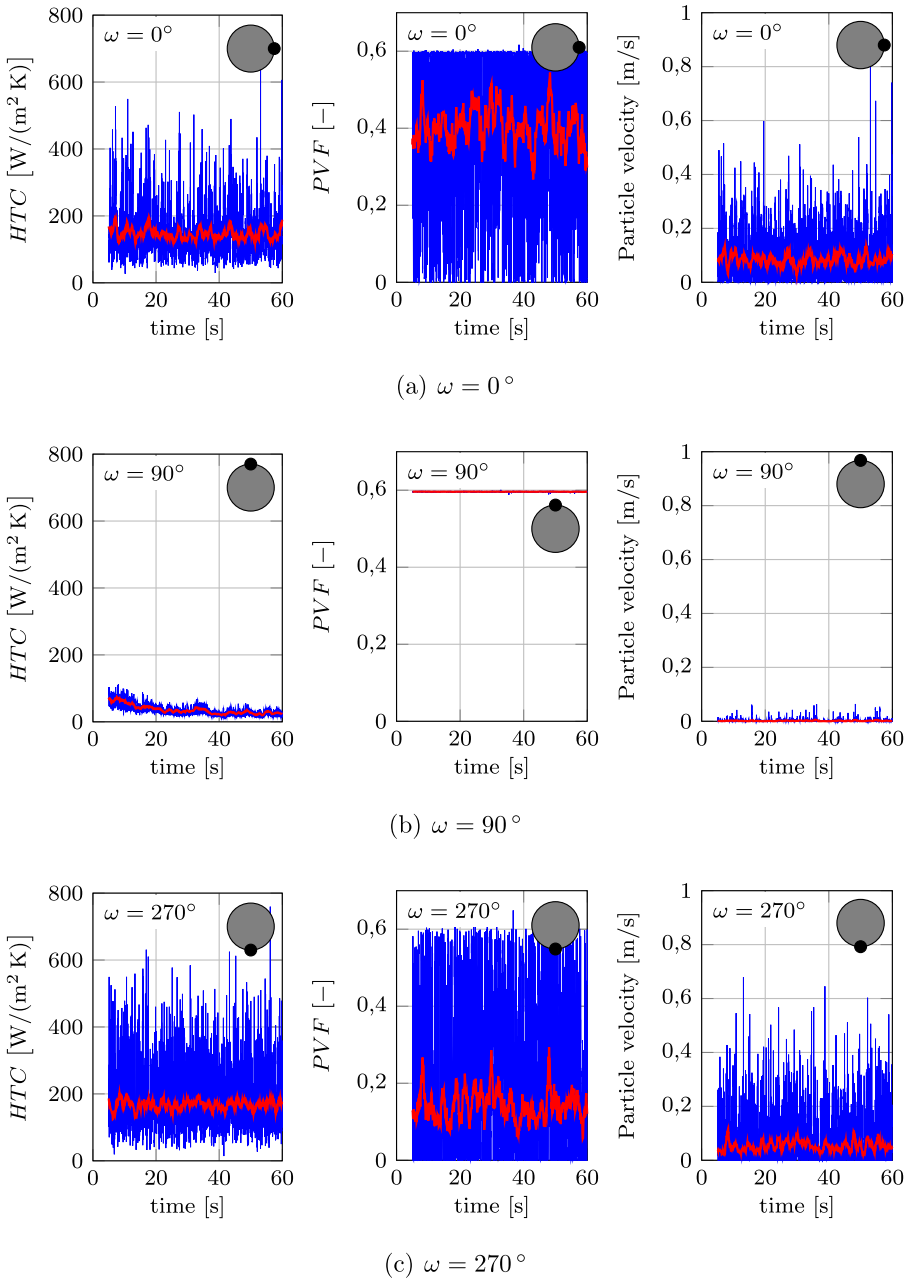

Fig. 4. Heat transfer coefficient (*HTC*), Particle volume fraction (*PVF*) and Particle velocity ($|\vec{u}_p|$) at different angular positions for the spherical surface. The blue line shows the raw data and the red line the moving average value every one second.

in the *HTC* related to cold particles entering into contact with this region of the surface, likely due to the action of ascending bubbles.

Fig. 7 for the cylindrical surface shows similar results to Fig. 6 for the sphere. These data indicate that the heat transfer mechanism differs depending on the angular position on the surface. The side of the surface is mainly surrounded by particles in the dense phase that moves slowly, while the bottom is in contact with particle-free gas bubbles. When a bubble travels around the heat transfer surface, the *HTC* augments instantaneously. At the top of the surface, the *HTC* remains low without significant variations because there are no bubbles in this zone.

These results help explain the values of the heat transfer coefficient (*HTC*) obtained at the wall in both surfaces. As the particles on the top of the tube are stagnant and are not removed by bubbles, their temperature notably increases. In consequence, the heat transfer in that region is notably reduced because there is no renovation of the hot particles by new cold ones that absorb energy from the hot tube.

To properly understand the relationship between the particle volume fraction and velocity and the heat transfer coefficient, Fig. 8 and 9 show the normalized power spectral density (*PSD*) for the heat transfer coefficient *HTC*, particle volume fraction (*PVF*) and particle velocity $|\vec{u}_p|$ at different angular positions around the spherical and the cylindrical surfaces, respectively. The *PSD* was computed according to the methodology proposed by Acosta-Iborra et al. [51]. The PSD were obtained with the average spectrum from eight consecutive sections of the signal with 50 % overlapping and a Hamming window to smooth the signal at the section endpoints. In Fig. 8, it is clearly observed that at $\omega = 90\,^{\circ}$, on the top of the tube, there are no fluctuations of the heat transfer coefficient, although there are some variations of the *PVF* and

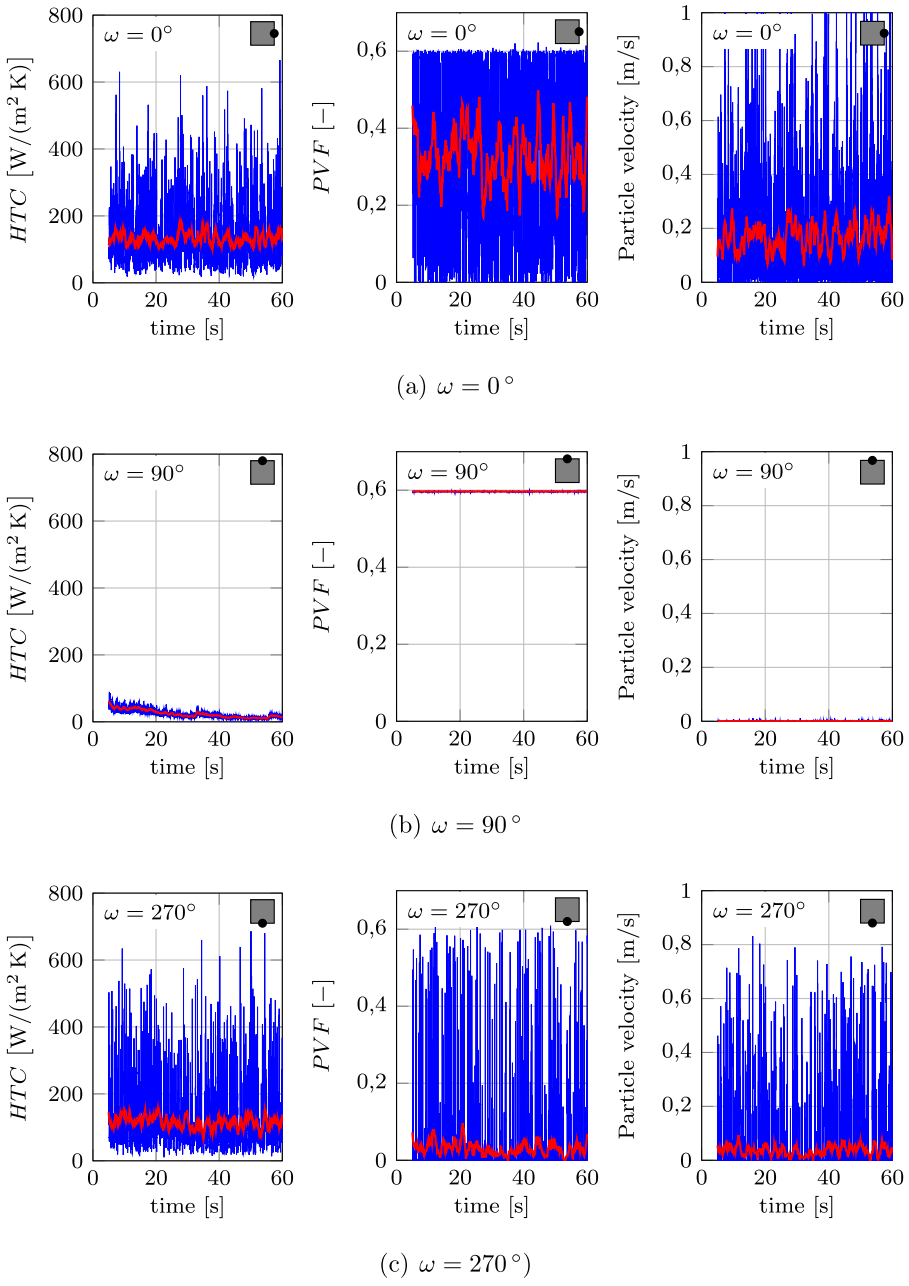

Fig. 5. Heat transfer coefficient (*HTC*), Particle volume fraction (*PVF*) and Particle velocity ($|\vec{u}_p|$) at different angular positions for the cylindrical surface. The blue line shows the raw data and the red line the moving average value every one second.

$\vec{u}_p$. Nevertheless, these variations are very small, as is shown in Fig. 4. The difference between the highest *HTC* value (0 °) and the lowest one (90 °) can be noted; this occurs with a transition at 45 ° in which the *PSD* of the *PVF* is changing. In contrast, at both sides of the tube ($\omega = 0$ ° and $\omega = 180$ °) the *PSD* of *HTC*, *PVF* and $|\vec{u}_p|$ are very similar at a dominant frequency of around 2-3 Hz, which is the bubble passing frequency at these points. As the bubbles pass, they move the heated particles on the surface and are replaced by new cold particles. This is the main mechanism for heat transfer at both sides of the tube. It should be noted that at $\omega = 45$ ° and $\omega = 135$ °, the *PVF* distribution is not symmetrical, which is related to a chaotic movement of bubbles. This might be improved by increasing the simulation time, although this would increase the computational cost. Finally, in the bottom region (225 ° $\leq \omega \leq$ 315 °), there are many more peaks of *HTC* for higher frequencies ($f \gtrsim 5$ Hz), which are not observed at the sides of the tube ($\omega = 0$ ° and 180 °). This, together with the low value of the *PVF* in this zone of the tube (see Figure 4), suggests a different heat transfer process in the bottom of the bed. Bubbles ascending through the bed likely drag some particles in their wake, which enter into contact with the bottom of the tube when the bubbles deviates to one side of the tube. This group of particles is less compact and moves at a lower velocity than the particles at the side of the tube. Note that the mean values of the *PVF* and $|\vec{u}_p|$ (Figs. 4(b) and 4(c)) for the data at $\omega = 0$ ° are 0.40 and 0.084 m/s, while at the bottom of the tube ($\omega = 270$ °) they are 0.14 and 0.054 m/s, respectively. In spite of these differences in the *PVF* and particle velocity, the averages in the time heat transfer coefficients are quite similar: 167.14 W/(m^2 K) and 146.73 W/(m^2 K) at $\omega = 0$ ° and 270 °, respectively. This could be related to the higher air velocity at the bottom of the bed, which could increase the fraction of the *HTC* related to the gas phase (h_f), although the fraction re-

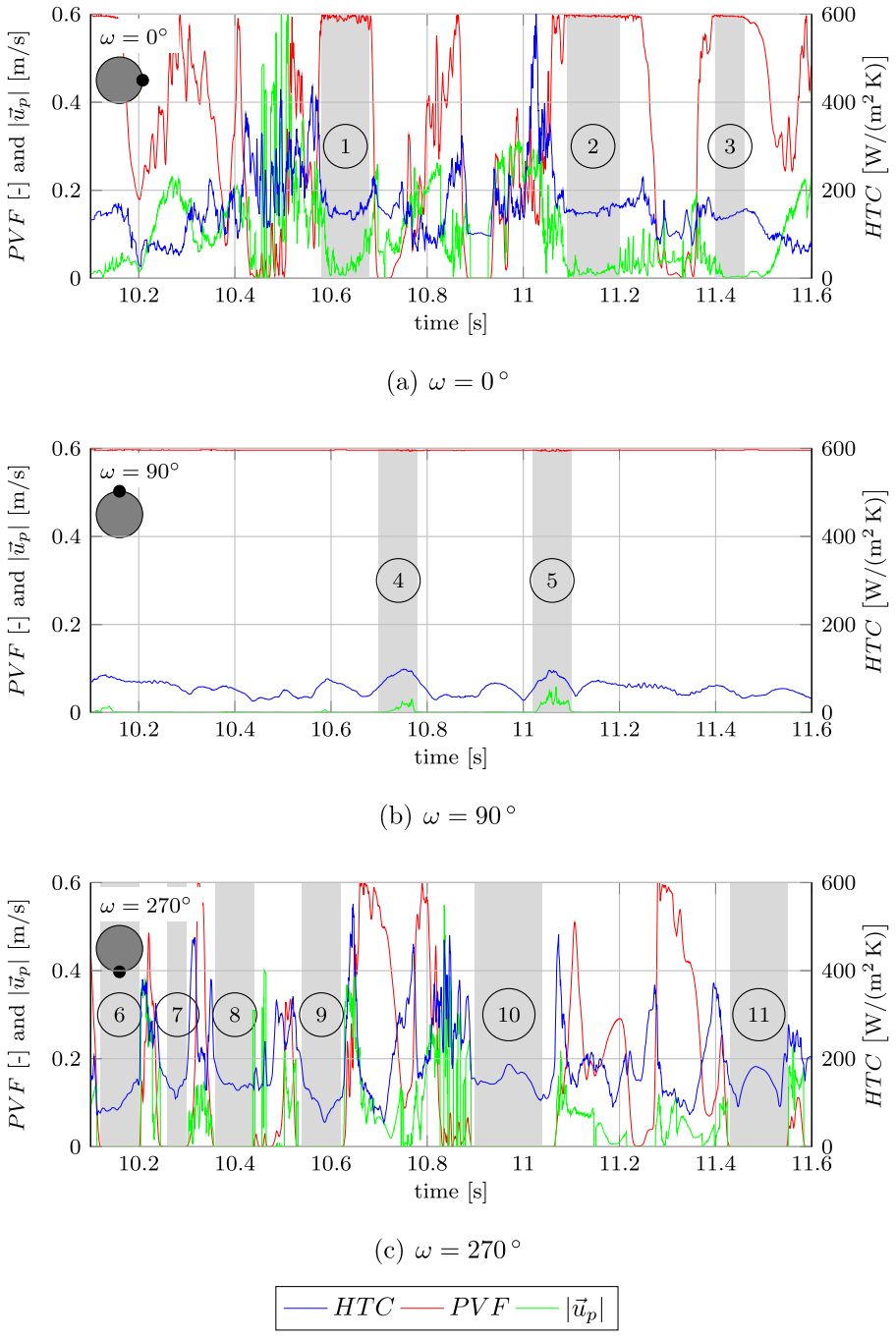

(a) $\omega = 0\,^\circ$

(b) $\omega = 90\,^\circ$

(c) $\omega = 270\,^\circ$

Fig. 6. Heat transfer coefficient (*HTC*), Particle volume fraction (*PVF*) and Particle velocity ($|\vec{u}_p|$) at different angular positions for the spherical surface.

lated to the motion of particles is reduced, i.e:

$$h_{f,\omega=0^\circ} < h_{f,\omega=270^\circ} \text{ and } h_{p,\omega=0^\circ} > h_{p,\omega=270^\circ} \tag{27}$$

Fig. 9 shows the same data for the cylindrical surface at the centre of the four sides of the surface. At the sides of the geometry ($\omega = 0^\circ$ and 180°) the results are similar and there is almost no difference between the three spectra: *HTC*, *PVF* and $|\vec{u}_p|$ show dominant peaks at frequencies around 2-3 Hz and the intensity of the peaks are progressively reduced for higher frequencies. At the top of the surface ($\omega = 90^\circ$), there is no variation in the *HTC*, as the particles are at rest, as is observed in Fig. 5. Finally, at the bottom ($\omega = 270^\circ$), there are higher peaks in the spectra at higher frequencies, compared to the cases at $\omega = 0^\circ$ and 180°. These higher frequencies are related to the impact of particles dragged by the bubbles continuously in contact with the bottom region of the bed. As in the case of the spherical geometry, the particle velocity and the *PVF* in this region are lower than at the sides of the geometry.

Fig. 10 and Table 5, show the average time values of the heat transfer coefficient ($\overline{HTC}_\omega$), particle volume fraction ($\overline{PVF}_\omega$)(Equation (28)) and particle velocity at different angular positions in the bed for the spherical and the cylindrical surfaces, respectively. For the spherical surface, it can be observed that the $\overline{PVF}_\omega$ is approximately symmetric with constant values close to $\overline{PVF}_\omega \approx PVF_{mf} \approx 0.6$ on the top of the bed ($30^\circ < \omega < 150^\circ$) and these values are reduced up to values close to $\overline{PVF}_\omega \approx 0.2$ on the

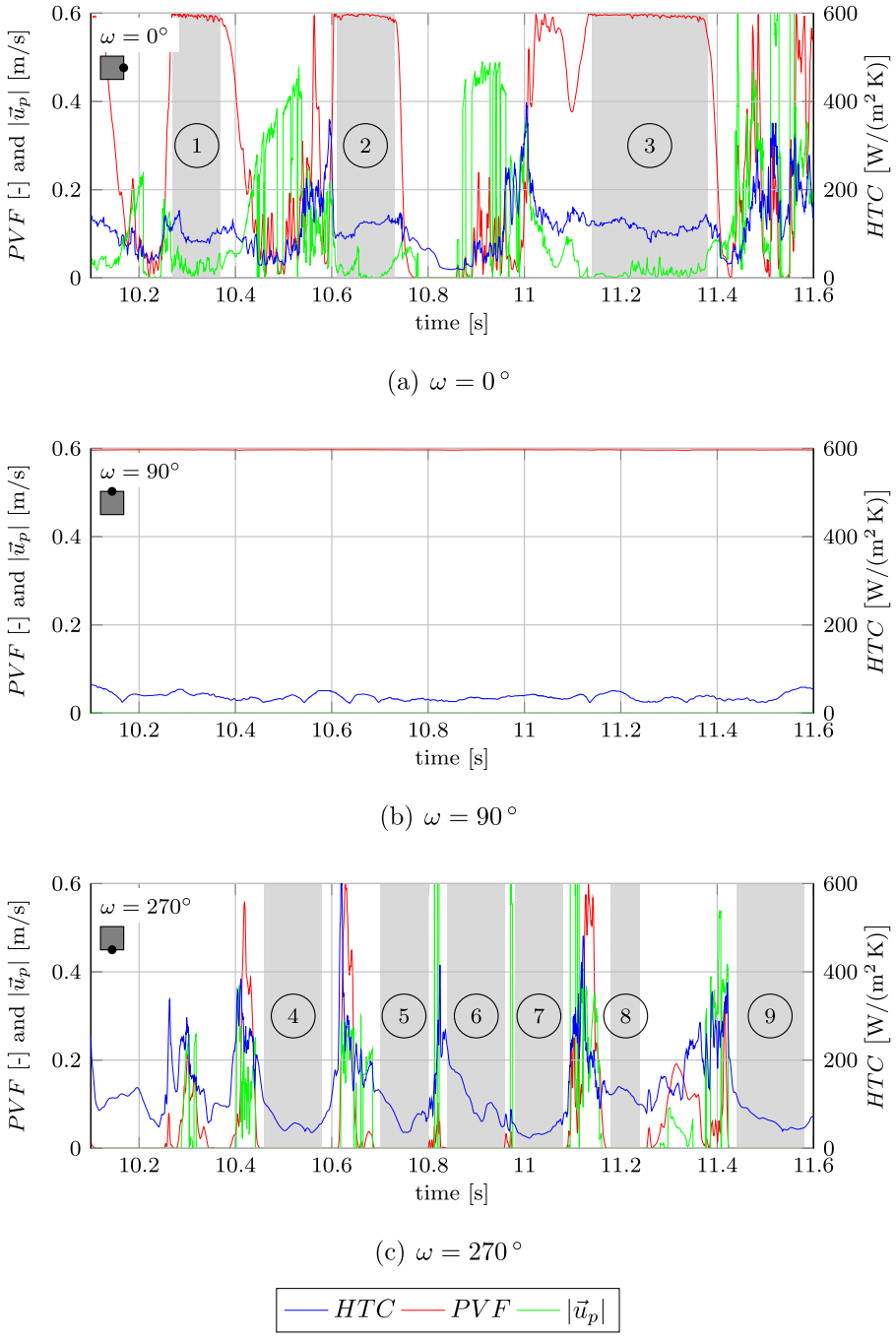

Fig. 7. Heat transfer coefficient (*HTC*), Particle volume fraction (*PVF*) and Particle velocity ($|\vec{u}_p|$) at different angular positions for the cylindrical surface.

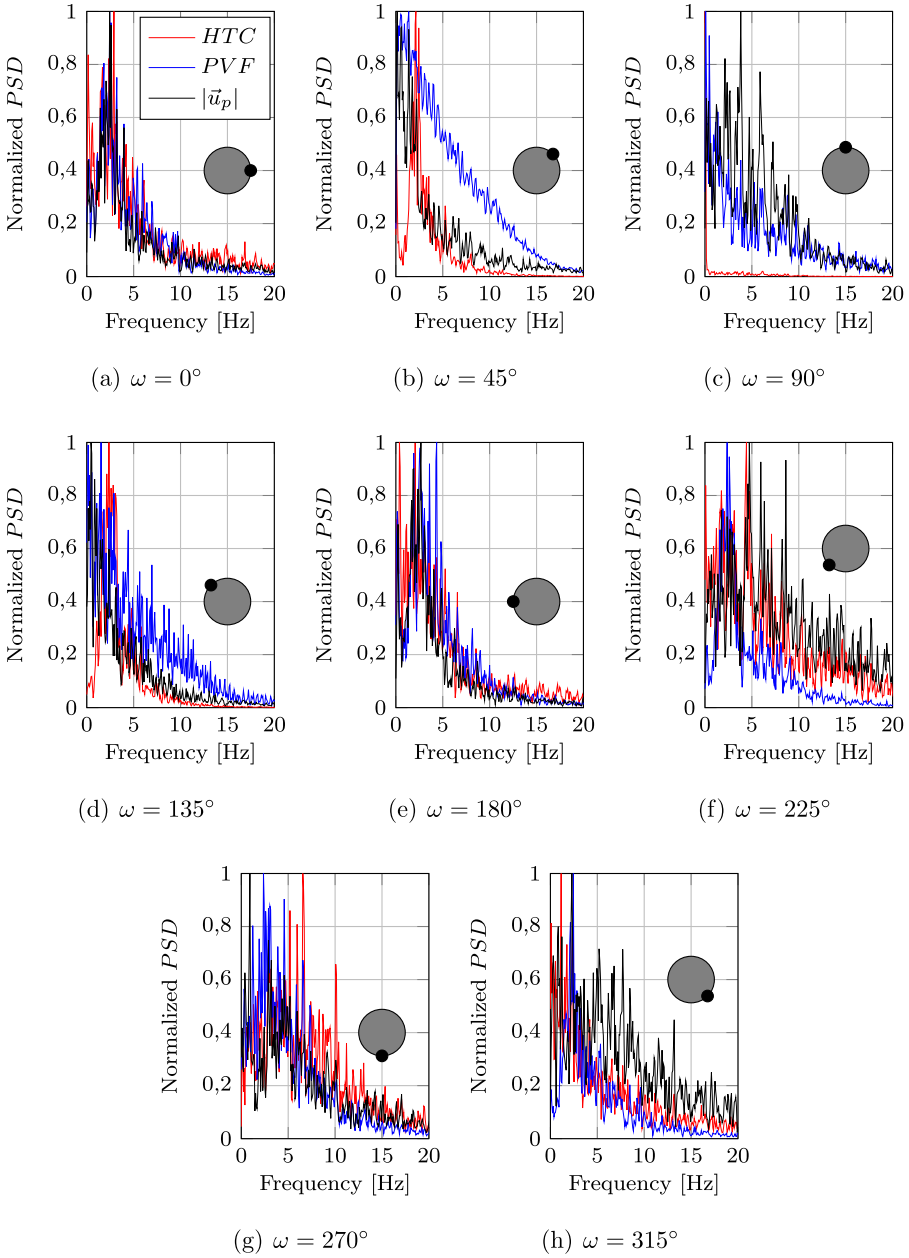

Fig. 8. Normalized Power Spectral Density (*PSD*) of the Heat transfer coefficient (*HTC*), Particle volume fraction (*PVF*) and Particle velocity ($|\vec{u}_p|$) at different angular positions for the spherical surface.

bottom ($210° < \omega < 330°$). The particle velocity is also symmetric with values close to zero at the top ($45° < \omega < 135°$) and maximum values close to 0.1 m/s at the sides of the surface ($\omega = 0°$ and $180°$). These high velocity regions are related to the bubbles passing around the tube surface and the particles displaced between bubbles. For the cylindrical geometry, however, the behaviour is different. The maximum heat transfer coefficients are located at the south corners of the surface ($\omega = 225°$ and $315°$), in exactly the position where the bubbles detach from the surface. This continuous motion of bubbles at this position is the responsible of the high heat transfer coefficient. The maximum particle velocities are also observed at the sides of the surface, close to the positions of the maximum $\overline{HTC}_\omega$. These maximum velocities are close to 0.2 m/s, which is approximately double that in the spherical surface.

$$\overline{PVF}_\omega = \frac{1}{t}\int_0^t \theta_p \, dt \tag{28}$$

In both the circular and the square geometries, the results for the local *HTC* obtained at the top surface is slightly different to the results obtained by previous studies analysing the same 2-D model but using *TFM*. In [22], the authors reported that, due to the formation and the heterogeneous flow of the bubbles around the tube, the distributions of the *PVF* and local heat transfer varied with time. Hence, at the top of the spherical surface, in three analysed simulation times (5, 6 and 7 s), they reported a maximum constant *PVF* value of 0.6. However, the *HTC* showed low values, apart from at 6 s, where the maximum *HTC* value was obtained. With regard to the cylindrical surface, the *PVF* also reached maximum constant values of 0.6 at the top, but only low *HTC* values were reached at 7 s, increasing at 5 and 6 s. In the study performed by [34], the authors concluded that the maximum *HTC* and *PVF* occurred at the top of both the spherical and the cylindrical surfaces. With regard to the results obtained using *CPFD – Barracuda*, this tendency at the top of the geometries is not ob-

Table 5
Time average values and standard deviation of the *HTC*, *PVF* and particle velocity for the spherical and cylindrical surface at different angular positions.

	Spherical surface							
	ω							
	0°	45°	90°	135°	180°	225°	270°	315°
$\overline{HTC}_\omega$ [W/(m² K)]	146.7	116.7	35.7	144.2	200.6	228.1	167.1	146.3
$\sigma_{\overline{HTC}_\omega}$ [W/(m² K)]	60.6	34.8	16.1	41.5	73.5	98.3	82.0	55.2
$\overline{PVF}_\omega$ [−]	0.403	0.594	0.596	0.592	0.405	0.205	0.142	0.176
$\sigma_{\overline{PVF}_\omega}$ [−]	0.209	0.018	0.001	0.027	0.208	0.238	0.188	0.233
$\bar{u}_p$ [m/s]	0.084	0.004	0.002	0.008	0.097	0.037	0.054	0.036
σ_{u_p} [m/s]	0.090	0.010	0.005	0.016	0.103	0.066	0.088	0.063
	Cylindrical surface							
	ω							
	0°	45°	90°	135°	180°	225°	270°	315°
$\overline{HTC}_\omega$ [W/(m² K)]	132.8	-	23.7	-	191.0	-	115.4	-
$\sigma_{\overline{HTC}_\omega}$ [W/(m² K)]	76.9	-	12.9	-	106.0	-	81.8	-
$\overline{PVF}_\omega$ [−]	0.327	-	0.597	-	0.336	-	0.031	-
$\sigma_{\overline{PVF}_\omega}$ [−]	0.226	-	0.001	-	0.224	-	0.095	-
$\bar{u}_p$ [m/s]	0.169	-	0.001	-	0.184	-	0.036	-
σ_{u_p} [m/s]	0.196	-	0.001	-	0.206	-	0.117	-

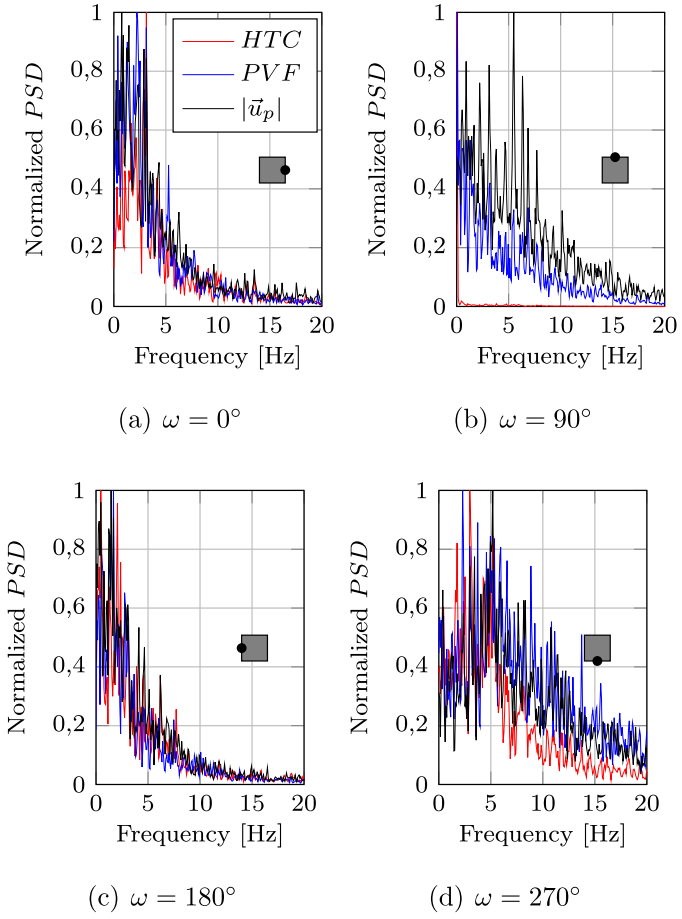

Fig. 9. Normalized Power Spectral Density (*PSD*) of the Heat transfer coefficient (*HTC*), Particle volume fraction (*PVF*) and Particle velocity ($|\vec{u}_p|$) at different angular positions for the cylindrical surface.

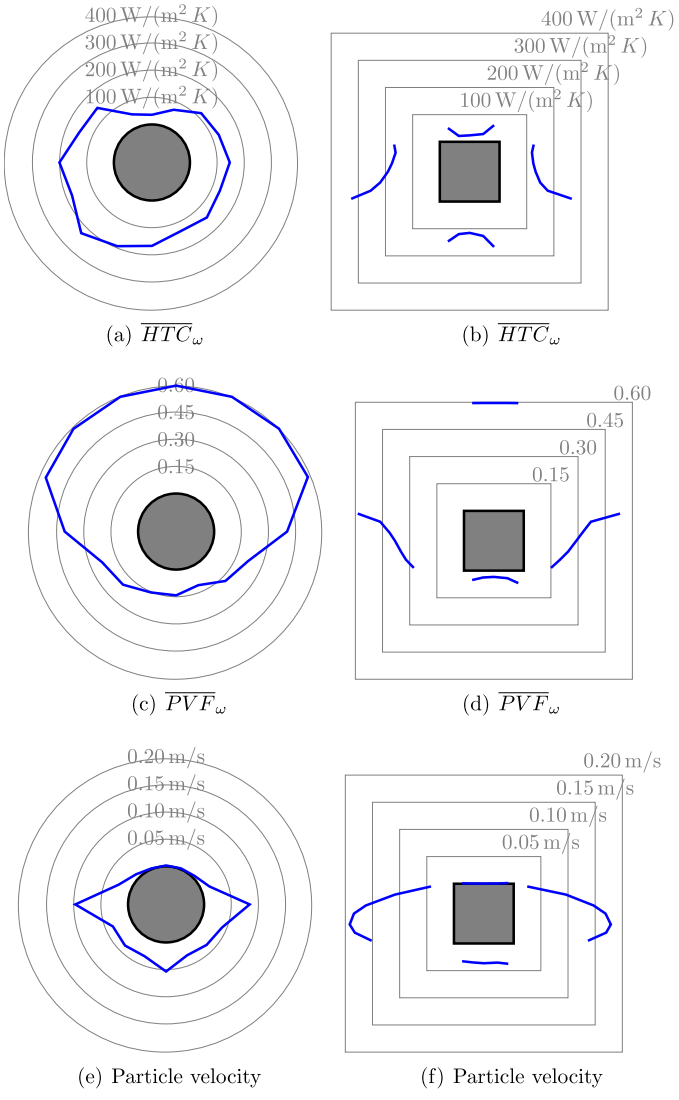

Fig. 10. Time average heat transfer coefficient, particle volume fraction and particle velocity at specified locations of the spherical and cylindrical probe surface

tained. In fact, during the simulation time, both *PVF* and *HTC* are approximately constant, reaching high and low values, respectively.

Fig. 11 shows the *HTC* versus *PVF* and u_p for both geometries at different angular positions. The data are the moving mean values during one second for the period 5 s < t < 60 s. Different regions of

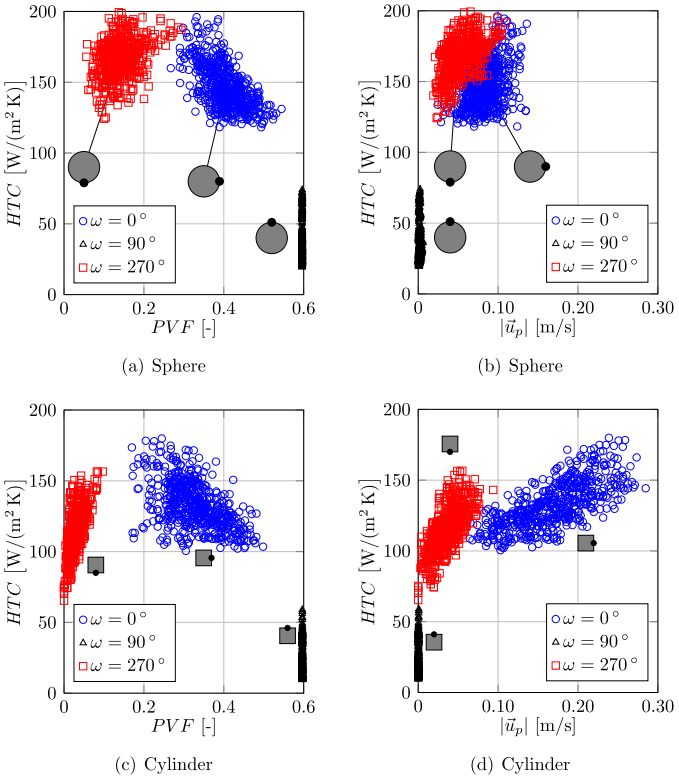

Fig. 11. Moving mean values during 1 second of *HTC* versus *PVF* and particle velocity for the spherical and the cylindrical surfaces at different angular positions.

points can be clearly distinguished, depending on the angular position. In general, data for $\omega = 0^\circ$ have higher values of *PVF* and u_p than $\omega = 270^\circ$. The differences in u_p are higher in the cylindrical geometry than in the spherical one, due to the sharp edges of the geometry. These figures show that the side of the heat transfer surface is mainly surrounded by particles of the dense phase with high values of *PVF*, whereas the bottom is mainly in contact with gas bubbles without particles, which results in low *PVF* values. On the top of the heat transfer surface, there are compact particles at rest.

4. Conclusions

Some discrepancies were obtained when comparing the simulation results with experimental data and simulations using *TFM*, regarding the value of the time average heat transfer coefficient. This might be related to the simplification of the geometry, i.e. approximation of both geometries to a 2-D model. Thus, a fully 3-D model might be more appropriate to obtain heat transfer coefficients resembling the experimental ones. In this regard, the CPFD-Barracuda simulations underpredicted the experimental heat transfer coefficient, reporting differences ranging from 25 % and 38 % for the cylindrical and the spherical surfaces, respectively. However, these differences were lower than those obtained by the two-fluid model approach with a 2-D model, which overpredicted the experimental heat transfer coefficient, with differences ranging from 110 % and 135 % for the spherical and the cylindrical shapes, respectively.

When comparing both geometries, it can be noted that the influence of the cylindrical shape on particle volume fraction distribution is slightly higher than the spherical surface, due to the abrupt shape of the surface, although no significant differences were found. Moreover, the bubble detachment is slightly faster on the spherical surface than in the cylindrical one. Regarding the spherical surface, it is worth noting the difference between the highest heat transfer coefficient value (at $\omega = 0^\circ$) and the lowest one (at $\omega = 90^\circ$), due to a transition at $\omega = 45^\circ$ in which the power spectral density of the particle volume fraction is changing.

The simulations performed in the present work show the influence of the hydrodynamics on the heat transfer phenomena, where the bubble formation affects the local heat transfer coefficient, which is highly dependent on its location at the tube surface. The numerical results indicate that CPFD-Barracuda is able to properly simulate the heat transfer and the dynamics of the bed in defluidized regions, such as on the top of an immersed surface, where the two-fluid model fails and overpredicts the heat transfer rate. The above results show that CPFD-Barracuda is, in general, able to predict the behaviour of bubbling beds with reasonable accuracy and with a relatively low computational cost.

The simulations carried out with CPFD-Barracuda were useful to highlight details of the hydrodynamics and heat transfer process with immersed surfaces, to better explain the fluidization process phenomena, especially in local regions of the computational domain, which is one of the main limitations of experimental studies. The CPFD-Barracuda simulations were also able to predict particle and gas behaviour at the top of the surfaces, in which the *TFM* does not accurately reproduce the fluidization mechanism and tends to overpredict the local heat transfer in that region, increasing the global heat transfer coefficient. These results show that the time average heat transfer coefficient at the top surface is 65 % and 77 % lower than the heat transfer coefficient over the whole heat transfer surface, for the spherical and the cylindrical surfaces, respectively.

5. Notation

A_p	Projected area of the particle [m^2]
A_s	Immersed surface area [m^2]
C_d	Gas-particle drag coefficient
CFL	Courant-Friedrichs-Lewy
CFD	Computational fluid dynamics
Cp_f	Fluid specific heat [$J/(kgK)$]
Cp_p	Specific heat of the particle [$J/(kgK)$]
$CPFD$	Computational particle fluid dynamic
DEM	Discrete element models
DPS	Discrete particle simulation
D_c	Cylindrical probe diameter [mm]
D_p	Drag function
D_s	Spherical probe diameter [mm]
d_p	Particle diameter [mm]
e_s	Particle-particle restitution coefficient
e_w	Wall to particle restitution coefficient
F	Momentum exchange rate per volume between gas and particles [N/m^3]
F_p	Drag force exerted on the particles [N]
f	Particle probability distribution function
f_p	Function of the particle volume fraction at the wall
g	Gravity acceleration [m/s^2]
H	Height [mm]
H_{bed}	Initial bed height [mm]
$\overline{h}_f$	Average convective heat transfer coefficient of the gas in the bubble phase [$W/(m^2 K)$]
h_f	Heat transfer coefficient of the gas[$W/(m^2 K)$]
h_{fe}	Fluid enthalpy [J/kg]
h_{fp}	Fluid-to-particle heat transfer coefficient [$W/(m^2 K)$]
H_{probe}	Immersed probe height [mm]
h_p	Instantaneous convective heat transfer coefficient of the particles [$W/(m^2 K)$]
$\overline{h}_p$	Average convective heat transfer coefficient of the particles [$W/(m^2 K)$]
h_{pe}	Particle enthalpy [J/kg]
HTC	Heat transfer coefficient [$W/(m^2 K)$]
HTC_m	Average heat transfer coefficient over the heat transfer surface [$W/(m^2 K)$]
$\overline{HTC}_m$	Time average heat transfer coefficient over the heat transfer surface [$W/(m^2 K)$]

$\overline{HTC}_{\omega}$	Time average heat transfer coefficient at angular position $\omega[W/(m^2 K)]$
h_w	Local fluid-to-wall heat transfer coefficient $[W/(m^2 K)]$
$\bar{h}_w$	Average fluid-to-wall heat transfer coefficient $[W/(m^2 K)]$
k_f	Fluid thermal conductivity $[W/(mK)]$
k_p	Particle thermal conductivity $[W/(mK)]$
L	Cell length $[m]$
L_c	Cylindrical probe length side [mm]
$MP-PIC$	Multiphase particle-in-cell
m_p	Particle mass [kg]
Nu_f	Nusselt number for heat transfer in the fluid to the particle
p	Fluid pressure [Pa]
PCM	Phase change material
PSD	Power spectral density
P_{out}	Pressure outlet [Pa]
P_s	Pressure constant
$\overline{PVF}_{\omega}$	Average in time particle volume fraction at angular position ω
PVF_{mf}	Particle volume fraction at minimum fluidization
q	Fluid heat flux $[W/m^2]$
$\dot{q}_D$	Enthalpy diffusion term associated with chemical reactions $[W/m^3]$
$\dot{Q}$	Energy source per volume $[W/m^3]$
R_g	Gas constant $[J/(kgK)]$
Re	Reynolds number
Sh	Conservative energy exchange from the particle phase to the fluid phase $[W/m^3]$
T	Absolute temperature [K]
TES	Thermal energy storage
T_f	Fluid temperature [K]
TFM	Two-fluid models
t_p	Residence time of the particles in contact with the heating surface [s]
T_s	Wall immersed surface temperature [K]
T_p	Particle temperature [K]
T_{wb}	Wall bed temperature [K]
u_f	Gas velocity [m/s]
u_{mf}	Minimum fluidization velocity [m/s]
u_p	Particle velocity [m/s]
$u_{p,z}$	Particles z-velocity [m/s]
V_p	Particle volume $[m^3]$
W	Width [mm]

5.1. Greek symbols

δ_w	Fraction of bubbles at the wall of the heat surface
θ_p	Particle volume fraction (PVF)
β	Constant
θ_{cp}	Particle volume fraction at close packing
ε	Constant
μ_f	Dynamic viscosity of the fluid $[kg/(m\,s)]$
ρ_f	Fluid density $[kg/m^3]$
ρ_p	Particle density $[kg/m^3]$
Ψ_p	Sphericity
θ_f	Fluid volume fraction
τ_f	Fluid stress tensor [Pa]
τ_p	Particle normal stress [Pa]
ω	Angular position [degrees]
Φ	Viscous dissipation $[W/m^3]$

Declaration of Competing Interest

The authors declare that they have no known competing financial interests or personal relationships that could have appeared to influence the work reported in this paper.

CRediT authorship contribution statement

J.I. Córcoles: Conceptualization, Methodology, Software, Validation, Formal analysis, Data curation, Writing - original draft, Writing - review & editing, Visualization. **A. Acosta-Iborra:** Conceptualization, Methodology, Validation, Formal analysis, Writing - original draft, Writing - review & editing. **J.A. Almendros-Ibáñez:** Conceptualization, Methodology, Validation, Formal analysis, Data curation, Writing - original draft, Writing - review & editing, Visualization, Supervision, Project administration, Funding acquisition.

Acknowledgments

The work was partially funded by the Spanish government (project ENE2016 - 78908 - R), the regional government of Castilla-La Mancha (project SBPLY / 17 / 180501 / 000412) and the Ministerio de Ciencia, Innovación y Universidades - Agencia Estatal de Investigación (AEI) (RED2018 - 102431 - T). One of the authors would like to acknowledge the financial support of *Comunidad de Madrid* and European Structural Funds through the ACES2030-CM project ($S2018/EMT-4319$) and Carlos III University of Madrid through the project *AccionEstrategica* ($Ref.2013/00179/002$).

Supplementary material

Supplementary material associated with this article can be found, in the online version, at doi:10.1016/j.ijheatmasstransfer.2021.121621

References

[1] X. Zeng, F. Wang, H. Li, Y. Wang, L. Dong, J. Yu, G. Xu, Pilot verification of a low-tar two-stage coal gasification process with a fluidized bed pyrolyzer and fixed bed gasifier, Applied energy 115 (2014) 9–16.
[2] Y. Liang, Y. Zhang, T. Li, C. Lu, A critical validation study on CPFD model in simulating gas–solid bubbling fluidized beds, Powder Technology 263 (2014) 121–134.
[3] M. Nakhaei, C.E. Hessel, H. Wu, D. Grévain, S. Zakrzewski, L.S. Jensen, P. Glarborg, K. Dam-Johansen, Experimental and CPFD study of gas–solid flow in a cold pilot calciner, Powder Technology 340 (2018) 99–115.
[4] Y. Yukselenturk, B. Yilmaz, Analysis of fluidization behavior in the loop-seal of a circulating fluidized bed gasifier using particle-in-cell method, Particulate Science and Technology 37 (8) (2019) 993–1006.
[5] Y. Wu, X. Shi, C. Wang, J. Gao, X. Lan, Cpfd simulation of hydrodynamics, heat transfer, and reactions in a downer reactor for coal pyrolysis with binary particles, Energy & Fuels 33 (12) (2019) 12295–12307.
[6] J.A. Almendros-Ibáñez, M. Fernández-Torrijos, M. Díaz-Heras, J.F. Belmonte, C. Sobrino, A review of solar thermal energy storage in beds of particles: packed and fluidized beds, Solar Energy 192 (2019) 193–237.
[7] A. Blaszczuk, M. Pogorzelec, T. Shimizu, Heat transfer characteristics in a large-scale bubbling fluidized bed with immersed horizontal tube bundles, Energy 162 (2018) 10–19.
[8] T. Khan, R. Turton, The measurement of instantaneous heat transfer coefficients around the circumference of a tube immersed in a high temperature fluidized bed, International journal of heat and mass transfer 35 (12) (1992) 3397–3406.
[9] A.I. Karamavruc, N.N. Clark, A correction factor for one-dimensional heat transfer coefficients around a horizontal tube in a fluidized bed, Powder technology 86 (2) (1996) 209–217.
[10] A. Gungor, A study on the effects of operational parameters on bed-to-wall heat transfer, Applied thermal engineering 29 (11-12) (2009) 2280–2288.
[11] J.A. Doherty, R.S. Verma, S. Shrivastava, S.C. Saxena, Heat transfer from immersed horizontal tubes of different diameter in a gas-fluidized bed, Energy 11 (8) (1986) 773–783.
[12] L. Wang, P. Wu, Y. Zhang, J. Yang, L. Tong, X. Ni, Effects of solid particle properties on heat transfer between high-temperature gas fluidized bed and immersed surface, Applied Thermal Engineering 24 (14-15) (2004) 2145–2156.
[13] M.A. Izquierdo-Barrientos, C. Sobrino, J.A. Almendros-Ibáñez, Experimental heat transfer coefficients between a surface and fixed and fluidized beds with PCM, Applied Thermal Engineering 78 (2015) 373–379.
[14] S.W. Kim, J.Y. Ahn, S.D. Kim, D.H. Lee, Heat transfer and bubble characteristics in a fluidized bed with immersed horizontal tube bundle, International Journal of Heat and Mass Transfer 46 (3) (2003) 399–409.
[15] M. Merzsch, S. Lechner, H.J. Krautz, Heat-transfer from single horizontal tubes in fluidized beds: Influence of tube diameter, moisture and diameter-definition by geldart c fines content, Powder technology 235 (2013) 1038–1046.
[16] T.W. Asegehegn, M. Schreiber, H.J. Krautz, Investigation of bubble behavior in fluidized beds with and without immersed horizontal tubes using a digital image analysis technique, Powder Technology 210 (3) (2011) 248–260.
[17] F. Di Natale, P. Bareschino, R. Nigro, Heat transfer and void fraction profiles around a horizontal cylinder immersed in a bubbling fluidised bed, International Journal of Heat and Mass Transfer 53 (17-18) (2010) 3525–3532.
[18] H. Al-Ansary, A. El-Leathy, Z. Al-Suhaibani, S. Jeter, D. Sadowski, A. Alrished, M. Golob, Experimental study of a sand–air heat exchanger for use with a high-temperature solar gas turbine system, Journal of solar energy engineering 134 (4) (2012).

[19] T. Hiromi, Particles flow pattern around tube and local in moving heat transfer bed, AIChE Journal 42 (6) (1996) 1621–1626.
[20] J. Niegsch, D. Köneke, P.-M. Weinspach, Heat transfer and flow of bulk solids in a moving bed, Chemical Engineering and Processing: Process Intensification 33 (2) (1994) 73–89.
[21] P. Bartsch, S. Zunft, Granular flow around the horizontal tubes of a particle heat exchanger: DEM-simulation and experimental validation, Solar Energy 182 (2019) 48–56.
[22] N.H. Dong, L.M. Armstrong, S. Gu, K.H. Luo, Effect of tube shape on the hydrodynamics and tube-to-bed heat transfer in fluidized beds, Applied thermal engineering 60 (1-2) (2013) 472–479.
[23] D.M. Snider, S.M. Clark, P.J. O'Rourke, Eulerian–lagrangian method for three-dimensional thermal reacting flow with application to coal gasifiers, Chemical Engineering Science 66 (6) (2011) 1285–1295.
[24] N.G. Deen, M.V.S. Annaland, M.A. Van der Hoef, J. Kuipers, Review of discrete particle modeling of fluidized beds, Chemical Engineering Science 62 (1-2) (2007) 28–44.
[25] A. Schmidt, U. Renz, Eulerian computation of heat transfer in fluidized beds, Chemical engineering science 54 (22) (1999) 5515–5522.
[26] V. Mathiesen, T. Solberg, B.H. Hjertager, Predictions of gas-particle flow with an eulerian model including a realistic particle size distribution, Powder Technology 112 (1-2) (2000) 34–45.
[27] F.P. Di Maio, A. Di Renzo, D. Trevisan, Comparison of heat transfer models in DEM-CFD simulations of fluidized beds with an immersed probe, Powder technology 193 (3) (2009) 257–265.
[28] Y. Zhao, M. Jiang, Y. Liu, J. Zheng, Particle-scale simulation of the flow and heat transfer behaviors in fluidized bed with immersed tube, AIChE Journal 55 (12) (2009) 3109–3124.
[29] Q.F. Hou, Z.Y. Zhou, A.B. Yu, Computational study of heat transfer in a bubbling fluidized bed with a horizontal tube, AIChE journal 58 (5) (2012) 1422–1434.
[30] K. Qiu, F. Wu, S. Yang, K. Luo, K.K. Luo, J. Fan, Heat transfer and erosion mechanisms of an immersed tube in a bubbling fluidized bed: a LES–DEM approach, International Journal of Thermal Sciences 100 (2016) 357–371.
[31] H. Wahyudi, K. Chu, A. Yu, 3d particle-scale modeling of gas–solids flow and heat transfer in fluidized beds with an immersed tube, International Journal of Heat and Mass Transfer 97 (2016) 521–537.
[32] T. Li, J.-F. Dietiker, Y. Zhang, M. Shahnam, Cartesian grid simulations of bubbling fluidized beds with a horizontal tube bundle, Chemical Engineering Science 66 (23) (2011) 6220–6231.
[33] R. Yusuf, B. Halvorsen, M.C. Melaaen, Eulerian–eulerian simulation of heat transfer between a gas–solid fluidized bed and an immersed tube-bank with horizontal tubes, Chemical engineering science 66 (8) (2011) 1550–1564.
[34] M. Fattahi, S.H. Hosseini, G. Ahmadi, A. Parvareh, Numerical simulation of heat transfer coefficient around different immersed bodies in a fluidized bed containing geldart b particles, International Journal of Heat and Mass Transfer 141 (2019) 353–366.
[35] P. Ostermeier, F. Dawo, A. Vandersickel, S. Gleis, H. Spliethoff, Numerical calculation of wall-to-bed heat transfer coefficients in geldart b bubbling fluidized beds with immersed horizontal tubes, Powder Technology 333 (2018) 193–208.
[36] Y. Zhang, Q. Wei, Cpfd simulation of bed-to-wall heat transfer in a gas-solids bubbling fluidized bed with an immersed vertical tube, Chemical Engineering and Processing: Process Intensification 116 (2017) 17–28.
[37] M. Leva, M. Grummer, A correlation of solids turnover in fluidized systems-its relation to heat transfer, Chemical Engineering Progress 48 (6) (1952) 307–313.
[38] F. Di Natale, A. Lancia, R. Nigro, Surface-to-bed heat transfer in fluidised beds: effect of surface shape, Powder technology 174 (3) (2007) 75–81.
[39] T.B. Anderson, R. Jackson, Fluid mechanical description of fluidized beds. equations of motion, Industrial & Engineering Chemistry Fundamentals 6 (4) (1967) 527–539.
[40] D.M. Snider, An incompressible three-dimensional multiphase particle-in-cell model for dense particle flows, Journal of Computational Physics 170 (2) (2001) 523–549.
[41] J.-H. Lim, K. Bae, J.-H. Shin, J.-H. Kim, D.-H. Lee, J.-H. Han, D.H. Lee, Effect of particle–particle interaction on the bed pressure drop and bubble flow by computational particle-fluid dynamics simulation of bubbling fluidized beds with shroud nozzle, Powder Technology 288 (2016) 315–323.
[42] F.A. Williams, Combustion theory benjamin, Cummings, Menlo Park (1985).
[43] P.J. O'Rourke, Collective drop effects on vaporizing liquid sprays, Technical Report, Los Alamos National Lab., NM (USA), 1981.
[44] D.M. Snider, S.M. Clark, P.J. O'Rourke, Eulerian–lagrangian method for three-dimensional thermal reacting flow with application to coal gasifiers, Chemical engineering science 66 (6) (2011) 1285–1295.
[45] C.Y. Wen, Mechanics of fluidization, in: Chem. Eng. Prog. Symp. Ser., volume 62, 1966, pp. 100–111.
[46] W.-c. Yang, Handbook of fluidization and fluid-particle systems, CRC press, 2003.
[47] W.J.M. Douglas, S.W. Churchill, Recorrelation of data for convective heat-transfer between cases and single cylinders with large termperature differences, Technical Report, 1955.
[48] R. Turton, T.J. Fitzgerald, O. Levenspiel, An experimental method to determine the heat transfer coefficient between fine fluidized particles and air via changes in magnetic properties, International journal of heat and mass transfer 32 (2) (1989) 289–296.
[49] M. Sommerfeld, N. Huber, Experimental analysis and modelling of particle-wall collisions, International journal of multiphase flow 25 (6-7) (1999) 1457–1489.
[50] S. Kraft, M. Kuba, F. Kirnbauer, K. Bosch, H. Hofbauer, Optimization of a 50 MW bubbling fluidized bed biomass combustion chamber by means of computational particle fluid dynamics, Biomass and Bioenergy 89 (2016) 31–39.
[51] A. Acosta-Iborra, C. Sobrino, F. Hernández-Jiménez, M. De Vega, Experimental and computational study on the bubble behavior in a 3-D fluidized bed, Chemical Engineering Science 66 (15) (2011) 3499–3512.